ADVANCED MATERIALS INTERFACES
Open Access
www.advmatinterfaces.de

Graphene Decorated With Mo_3S_7 Clusters for Sensing CO_2

Juan Casanova-Chafer, Eduard Llobet, and Marta Feliz**

This paper reports for the first time a gas-sensitive nanohybrid based on trinuclear molybdenum sulfido clusters ($(Bu_4N)_2[Mo_3(\mu_3\text{-}S)(\mu\text{-}S_2)_3Cl_6]$ (Mo_3S_7)) supported on graphene flakes (Mo_3S_7@Graphene). The nanomaterial, once implemented in a chemoresistive device, changes its electrical resistivity when exposed, at room temperature (RT), to toxic and harmful gases, such as hydrogen (H_2), carbon dioxide (CO_2), carbon monoxide (CO), and benzene. Particularly, the Mo_3S_7@Graphene hybrid shows an outstanding sensing performance toward CO_2. Theoretical calculations provide a better understanding of the plausible gas sensing mechanisms. These findings open the door for a new generation of molybdenum sulfido cluster-based sensors in which electronic interrogation can be implemented, advancing toward the realization of highly sensitive gas sensing.

1. Introduction

The control of air pollutants' impact on the environment and human health requires accurate monitoring of atmospheric ambient conditions.[1] Conventional air quality monitoring methods, such as gas chromatography (GC), involve stationary and costly equipment, limiting monitoring point' density. However, deploying a dense network of affordable sensors can provide real-time and comprehensive air pollutant distribution maps, essential for identifying pollution sources, understanding dispersion patterns, and assessing exposure levels in different areas.[2] Therefore, the development of cost-effective, miniaturized sensors, operable at RT to reduce power consumption, maintenance frequency, and replacement costs, is crucial.[3]

Chemiresistive gas sensors have advantages like simplicity and cost-effectiveness over other gas sensing technologies.[4] While GC is highly accurate and capable of detecting various gases at low concentrations, it is expensive, requires complex instrumentation, and is not suitable for real-time or in situ monitoring due to sample preparation and longer analysis time. Chemiresistive gas sensors are better suited for continuous, real-time monitoring, based on the principle that the electrical resistance of a sensing material changes when it interacts with target gas molecules. This resistance change can be easily measured and correlated to the gas concentration, enabling rapid pollutant detection.[5]

In recent years, molybdenum chalcogenides and their derivatives have been extensively explored for pollutant gas detection.[6–12] The derived nanostructured semiconductors vary in composition and morphology, which impacts sensing performance. The fabrication of molybdenum sensors is highly attractive due to its abundant availability and low toxicity, with the development of thin films and nanoparticles being the most prevalent approaches.[13] For instance, T. Pham and collaborators developed a MoS_2 sensor capable of detecting a few ppb of NO_2,[14] while $MoSe_2$ nanosheets have been demonstrated as a suitable option for the rapid detection of a few ppm of NH_3.[15] Nevertheless, developing new molybdenum materials with advanced properties for large-scale fabrication is still incipient.

In 2022, we reported the first development of Mo_6 clusters supported on graphene for detecting gases such as NO_2 and NH_3.[16] However, the development of nanocomposites composed of graphene and molybdenum sulfido clusters for gas sensing purposes has not yet been reported. These nanomaterials include heterogeneous hybrids composed of architectured molecular components, including a trinuclear molybdenum sulfido cluster with a $[Mo_3(\mu_3\text{-}S)(\mu\text{-}S_2)_3]^{4+}$ cluster core. The topology of this cluster unit is approximately C_{3v} symmetrical (**Scheme 1**). It comprises three Mo(IV) atoms distributed into an equilateral triangle capped by one central or apical μ_3-sulfido ($(S^{2-})^{ap}$), with each side of the metal triangle bridged by a μ-disulfido group ($(S_2{}^{2-})^{br}$). The disulfido bridges are oriented perpendicular to the Mo_3 triangle with the two inequivalent sulfur atoms occupying an equatorial (S_{eq}, in-plane) and an axial (S_{ax}, out-of plane) position. These metal cluster compounds represent a robust and extensive class

J. Casanova-Chafer
ChIPS Research Group
Department of Chemistry
Université de Mons
Mons 7000, Belgium
E-mail: juan.casanovachafer@umons.ac.be

E. Llobet
MINOS Research Group
Department of Electronics Engineering
Universitat Rovira i Virgili
Tarragona 43007, Spain

M. Feliz
Instituto de Tecnología Química (Universitat Politècnica de València – Agencia Estatal Consejo Superior de Investigaciones Científicas)
Avd. de los Naranjos s/n, Valencia 46022, Spain
E-mail: mfeliz@itq.upv.es

The ORCID identification number(s) for the author(s) of this article can be found under https://doi.org/10.1002/admi.202400590

DOI: 10.1002/admi.202400590

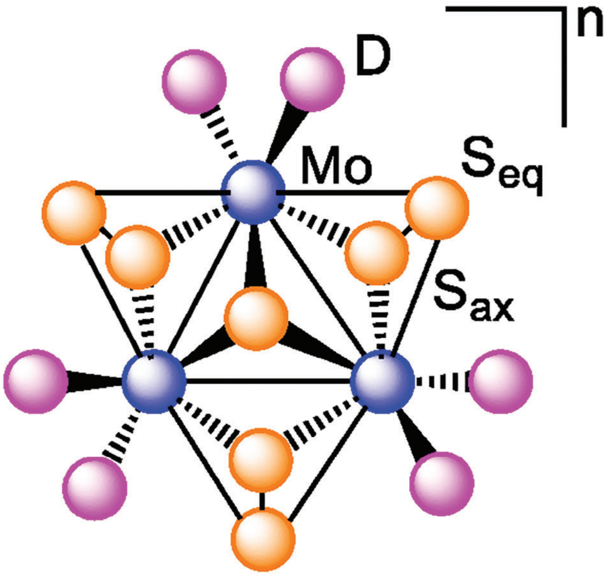

Scheme 1. Schematic representation of the $[Mo_3(\mu_3\text{-}S)^{ap}(\mu\text{-}S_2)^{br}{}_3D_6]^n$ cluster system, where n is the cluster charge, D corresponds to the donor atoms of a monodentate or bidentate ligand, “ap” and “br” refers to apical and bridging cluster positions, respectively, and “eq” and “ax” corresponds to equatorial and axial positions respect to the trimetallic plane.

of compounds with diverse coordination chemistry. The coordination sphere of each Mo atom is completed by six apical or terminal coordination sites that can be occupied by monodentate ligands, such as aqua or halido, or bidentate, such as disulfido or dithiolene, placed in *cis* and *trans* positions to the μ_3-sulfur atom. Their intrinsic optical and electronic properties have provided molecular, polymeric, and supported materials with interesting physical and chemical applications in optics, magnetic and electrical conductivity, and catalysis.[17–20] One of the most studied trinuclear molybdenum sulfido clusters with technological applications is the $[Mo_3(\mu_3\text{-}S)(\mu\text{-}S_2)_3(S_2)_3]^{2-}$ cluster compound. This $[Mo_3S_{13}]^{2-}$ cluster resulted in much interest in the catalytic field: some time ago, it was employed as a model for high-performance Mo–S catalysts of oil desulfurization,[21] and more recently, as an efficient active site in the field of hydrogen evolution reaction (HER) in homogeneous conditions,[22–24] or supported onto conductive organic supports.[25–28]

To the best of our knowledge, the use of $Mo_3(\mu_3\text{-}S)(\mu\text{-}S_2)_3$ clusters and their hybrid-supported materials for detecting pollutant species in the gas phase remains unexplored. While most research has focused on chemiresistive gas sensors based on metal oxides, dichalcogenides, and carbon structures,[3,7,29–32] this paper encompasses for the first time, the preparation of a Mo_3S_7@Graphene nanohybrid composed by trinuclear molybdenum sulfido clusters, with formula $(Bu_4N)_2[Mo_3(\mu_3\text{-}S)(\mu\text{-}S_2)_3Cl_6]$ (Mo_3S_7), supported on graphene, and the integration of this hybrid onto a transducing platform enabling chemoresistive gas sensing. The detection of four hazardous gaseous species has been investigated. H_2 is recognized as flammable and CO is a toxic gaseous species. Benzene is a highly toxic volatile organic compound (VOC), and CO_2 is considered potentially hazardous when present in high concentrations in the air. Besides reporting the sensing properties of the Mo_3S_7@Graphene hybrid nanomaterial, its thorough morphological and compositional characterization are reported as well. Finally, the cluster–gas interactions involved in the chemoresistive detection is analyzed computationally and a plausible detection mechanism is discussed.

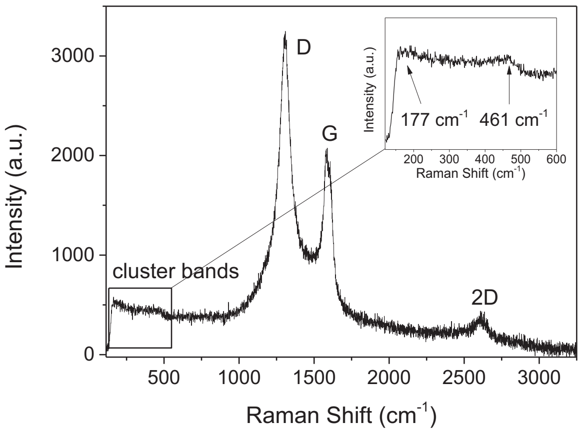

Figure 1. Raman spectrum of Mo_3S_7@Graphene hybrid. The bands identified at low Raman shifts (inset) are characteristic bands of the $[Mo_3(\mu_3\text{-}S)(\mu\text{-}S_2)_3]^{4+}$ cluster core material. The depicted spectrum was registered at 785 nm.

2. Results and Discussion

2.1. Nanomaterial Characterization

The crystalline Mo_3S_7 material and its derived nanohybrid (Mo_3S_7@Graphene) were prepared and characterized using several techniques such as Raman spectroscopy, powder X-ray diffraction, high-resolution field-emission scanning electron microscopy (HR-FESEM), high-resolution transmission electron microscopy (HR-TEM) and X-ray photoelectron spectroscopy (XPS). The synthesis of Mo_3S_7 was achieved by terminal disulfido/chlorido exchange reaction between $(NH_4)_2[Mo_3S_{13}]$ and hydrochloric acid, followed by counterion exchange with Bu_4NCl. The supported inorganic clusters at the graphene surface are essential in gas sensing performance, enabling higher interactions with gas compounds. The immobilization of Mo_3S_7 on graphene was done by mixing the respective precursors dispersed in dichloromethane, resulting in Mo_3S_7@Graphene. Raman spectra of this hybrid material were recorded at 514 and 785 nm. At 785 nm, the Raman region below 500 cm^{-1} shows two wide and low-intense bands (**Figure 1**), which can be ascribed to the vibrations of the molybdenum cluster precursor. Whereas Figure S1a (Supporting Information) shows intense bands in the spectrum of the molecular Mo_3S_7 material, with Raman shifts between 165 and 469 cm^{-1} characteristic of the Mo–Mo, Mo–S, and Mo-Cl vibrations of the cluster, the two intense bands at 561 and 570 cm^{-1}, mainly associated with the bridging disulfido ligands, are not detected in the Mo_3S_7@Graphene nanohybrid.[33] This could be due to the influence of the cluster anchoring in the electronic characteristics of the cluster core, instead of cluster desulfurization. At higher frequencies, the characteristic D, G, and 2D bands of graphene appear at 1305, 1584, and 2610 cm^{-1},

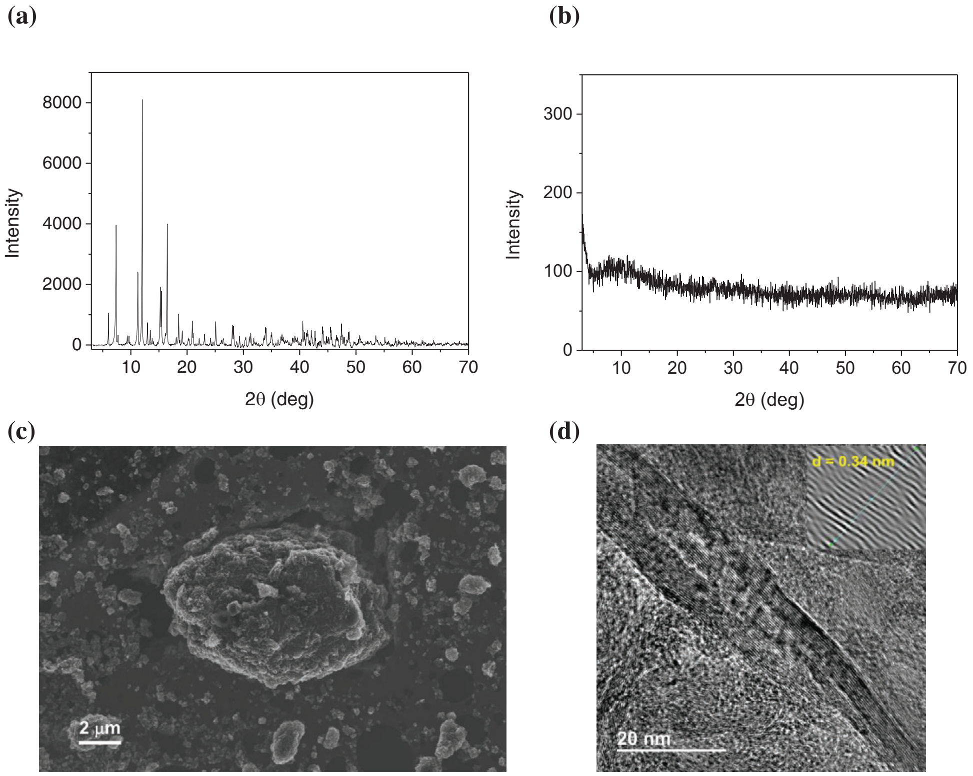

Figure 2. a) Powder X-ray diffractogram of the Mo_3S_7 material, b) powder X-ray diffractogram of the Mo_3S_7@Graphene sample, c) HR-FESEM and d) HR-TEM images of the sensor surface of the Mo_3S_7@Graphene material.

respectively. The D band is associated with structural defects, disordered carbon atoms in the sp^2 configuration, and carbonaceous impurities, while the G band is related to in-plane vibrations of sp^2 carbon bonds. Thereby, the D/G ratio revealed low crystalline graphene and the presence of defects and oxygenated functional groups grafted to the graphene probably supports the immobilization of molybdenum clusters. When the Raman spectrum of Mo_3S_7@Graphene was registered at 514 nm, the characteristic D, G and 2D graphene bands were detected, but under these conditions, the cluster region was inactive (Figure S2, Supporting Information). This could be associated with the lower intensity bands detected in the Raman spectra of Mo_3S_7 when a lower excitation wavelength is used (Figure S1b, Supporting Information). In both cases, the support drastically influences the detection of the characteristic cluster Raman pattern, and more identification tools are needed to prove the presence of trinuclear Mo clusters.

Powder X-ray diffraction confirmed the suitable cluster synthesis. **Figure 2**a illustrates the diffractogram of the Mo_3S_7 material, which is in accordance with the purity of the compound.[23] The X-ray pattern of Mo_3S_7@Graphene (Figure 2b) shows low crystallinity of graphene, and the absence of the diffraction peaks of the crystalline Mo cluster compound could suggest that the cluster is supported in molecular form. The morphology of the Mo_3S_7@Graphene nanomaterial was analyzed by textural and microscopic techniques. An HR-FESEM analysis (Figure 2c) shows the surface of the nanomaterial once it was deposited on the sensor surface, and HR-TEM (Figure 2d) confirms the laminar nature of the graphene nanosheets. Based on TEM analysis, an interlayer spacing of 0.34 nm is found, which is associated with multilayered graphene sheets.[34] Considering the thickness of the cluster anion (≈0.7 nm estimated from its structural analysis), the presence of the cluster complex between these graphene layers is not envisaged, which is consistent with the cluster supported on the graphene surface. All the attempts to determine the amount of the supported cluster atoms were unsuccessful. The low amount of Mo, S, and Cl is less than 1% w/w (below the limit of detection) prevents cluster identification and proper elemental quantification by these techniques.

The surfaces of the molecular trimetallic cluster and the Mo_3S_7@Graphene and graphene nanomaterials were characterized by XPS. The Mo and S regions are depicted in **Figure 3**. Deconvolution analyses of the molybdenum Mo 3d region show the Mo $3d_{5/2}$ and $3d_{3/2}$ peaks centered at 229.7 and 232.9 eV, respectively, which are almost identical to those observed for the starting Mo_3S_7 compound (229.4 eV for Mo $3d_{5/2}$ and 232.6 eV for Mo $3d_{3/2}$), all consistent with Mo(IV) oxidation state (Figure 3a,b). These results are similar to those reported for molecular $Mo_3(\mu_3\text{-}S)(\mu\text{-}S_2)_3$ species.[25,27,28,35–37] The almost identical Mo 3d binding energies (BEs) between the Mo_3S_7 and its supported material, and the absence of additional peaks associated with oxidized species indicate that the molybdenum cluster core remains intact after immobilization on the graphene surface in experimental conditions. An additional peak at 227.4 eV appears in the Mo 3d region of both materials, which is characteristic of S 2s band. The S 2p edge of the supported material shows a $2p_{3/2}$ and $2p_{1/2}$ doublet at 163.2 and 164.4 eV, respectively, which corresponds to

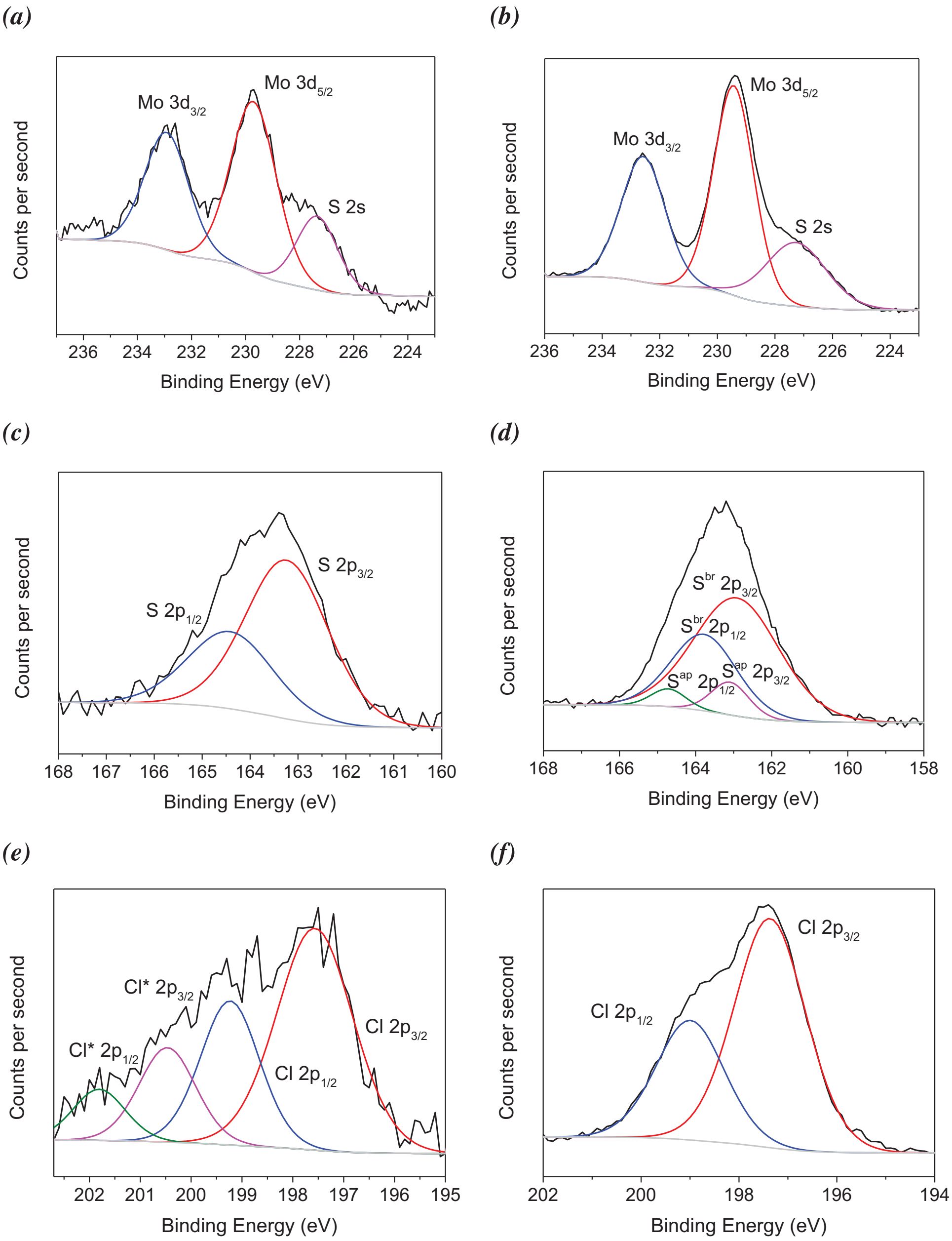

Figure 3. XPS Mo 3d (a, b), S 2p (c, d) and Cl 2p (e, f) regions of Mo_3S_7@Graphene (left) and Mo_3S_7 (right) materials.

apical and bridging sulfur ligands considering the BEs reported for $Mo_3(\mu_3\text{-}S)^{ap}(\mu\text{-}S_2)^{br}_3$ species (Figure 3c). For the Mo_3S_7 material (Figure 3d), the S 2p region provided two pairs of S $2p_{3/2}$ and $2p_{1/2}$ components: the most intense appears at 162.9 and 163.8 eV, and the less intense at 163.1 and 164.7 eV, respectively. A comparison between the identified $2p_{3/2}$ BEs and those reported in the literature indicates that the most intense doublet corresponds with bridging S_2^{2-} ligands, and the less intense with the apical S atom of the $Mo_3(\mu_3\text{-}S)^{ap}(\mu\text{-}S_2)^{br}_3$ unit.[36,37] The analysis of the atomic sulfur content of the two S 2p doublets shows a good correspondence between experimental (XPS) and theoretical S^{2-}/S_2^{2-} ligand ratio for the Mo_3S_7 material. The different shapes of the S 2p regions of the supported material versus the molecular one is mainly attributted to the cluster inmobilization. The Mo and S bands of the Mo_3S_7@Graphene material (Figure 3a,c) and the invariability of the atomic Mo/S ratio confirm the robustness of the $[Mo_3(\mu_3\text{-}S)(\mu\text{-}S_2)_3]^{4+}$ cluster core once deposited onto the graphene surface. In consequence, no desulfurization, polymerization or oxidation of the cluster core is observed after the cluster immobilization, in contrast to that reported for other $[Mo_3S_{13}]^{2-}$ cluster-based hybrid materials.[38,39]

The Cl 2p XPS region of the Mo_3S_7@Graphene nanohybrid (Figure 3e) shows two main $2p_{3/2}$ and $2p_{1/2}$ components at 197.6 and 199.2 eV, respectively, with a ≈2:1 area ratio, which are associated with the chlorido ligands of the molybdenum cluster (Figure 3f). Two additional Cl 2p components (labeled as

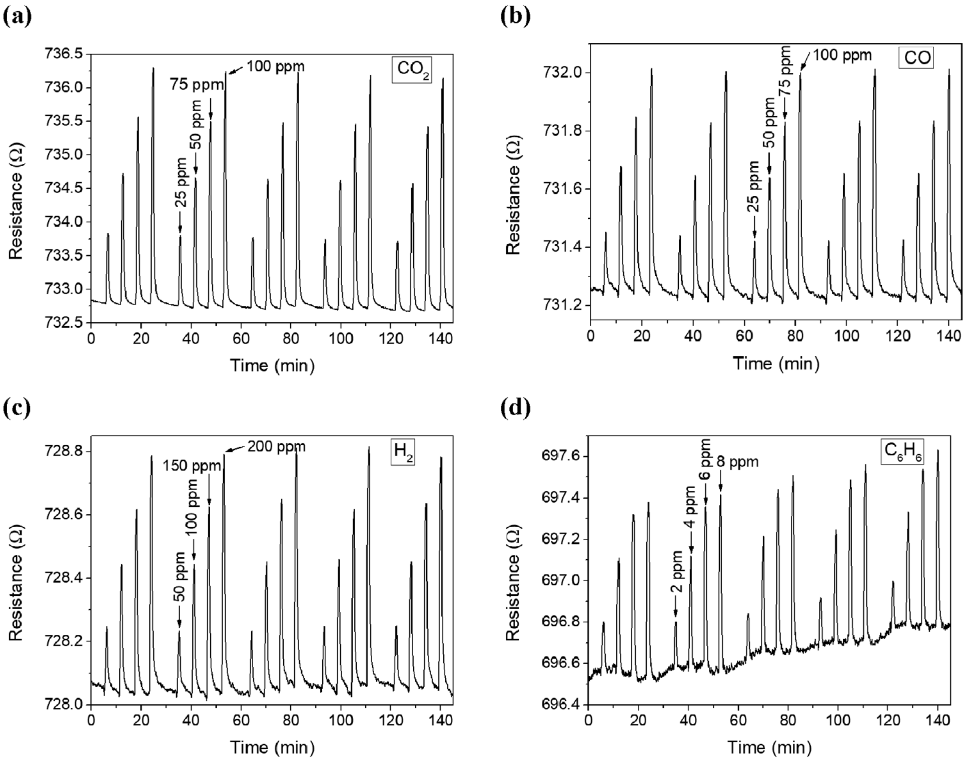

Figure 4. Electrical responses of the Mo_3S_7@Graphene to CO_2 (a), CO (b), H_2 (c), and benzene (d). Each gas was tested at four different concentrations, with measurements conducted over five consecutive cycles.

Cl* in Figure 3e) appear at 200.5 and 201.8 eV, consistent with a different chemical environment for chlorides. These components are not present in the XPS Cl region of the molecular cluster compound. Thus, a partial decoordination of chlorine atoms is envisaged after the cluster immobilization to give rise to the formation of [Mo-cluster···Cl*] adducts. This supramolecular cluster–chlorine interaction was reported structurally, and its formation was attributed to the electrophile character of the axial sulfur atoms of $Mo_3(\mu_3\text{-}S)(\mu\text{-}S_2)_3$ systems toward anionic counterions.[40–42] Interestingly, these BEs are similar to those described for $2p_{3/2}$ and $2p_{1/2}$ components of C-Cl bonds in chlorinated graphenes.[43,44] However, the anchoring of Cl atoms onto the graphenic surface is not envisaged, due to the soft reaction conditions used that contrast with those reported for Cl decoration of graphene, such as electrochemical, UV and heat-assisted conditions. This is evidenced by looking at the C 1s regions of the XPS spectra for Mo_3S_7@Graphene and graphene (Figure S3, Supporting Information), which are close in shape.

From the results obtained from the Cl 2p region of the XPS spectrum of Mo_3S_7@Graphene, it is inferred that the Mo_3 cluster is immobilized onto the graphene surface by coordinative interactions. Coordinative grafting of the cluster complex onto oxygen-functionalities of the graphene surface is envisaged. The low content of oxygen functionalities (less than 2% w/w) in the graphene support encompasses grafting functionalities, such as carboxyl or hydroxyl, that would interact with the trimetallic cluster because of the known lability of the halogen (X = Cl or Br) in $[Mo_3(\mu_3\text{-}S)(\mu\text{-}S_2)_3X_6]^{2-}$ cluster complexes. In general, the ligand metathesis can be achieved quantitatively, and partial ligand substitution has been reached in few cases by neutral ligands, such as DMSO, acetonitrile, aniline, or phenanthroline.[41,42,45,46] In this work, the Cl(Mo-cluster):Cl* atomic concentration (%) ratio calculated from the Cl 2p region of the Mo_3S_7@Graphene XPS spectrum is 76:24, which approximates the 5:1 atomic ratio relative to the chlorine content of the Mo_3S_7 compound. This quantitative analysis suggests that the exchange between one chlorido and one among the oxygen functionalities of the graphene support takes an active part in the grafting of the $Mo_3(\mu_3\text{-}S)(\mu\text{-}S_2)_3$ units.

2.2. Gas Detection using a Chemoresistive Transducing Scheme

The ability of the Mo_3S_7@Graphene layer to detect several gas species was evaluated under room temperature operational conditions. This methodology offers the advantage of low power consumption and reduced fabrication costs for the resulting devices. Four different gases were subjected to analysis: CO_2, CO, H_2, and benzene vapors, across varying analyte concentrations. **Figure 4a** shows the electrical responses of the Mo_3S_7@Graphene sensor to different CO_2 levels ranging from 25 to 100 ppm, recorded over five consecutive cycles. It can be observed that the Mo_3S_7@Graphene hybrid exhibits an outstanding signal-to-noise ratio, facilitating the effective measurement of CO_2 despite the limited absolute resistance changes. The development of new materials for CO_2 detection is still incipient, and the great sensitivity observed for the Mo_3S_7@Graphene hybrid toward CO_2 is extraordinary among the molybdenum sulfido composites.[6] Furthermore, **Figure 5a** compares the sensing performance

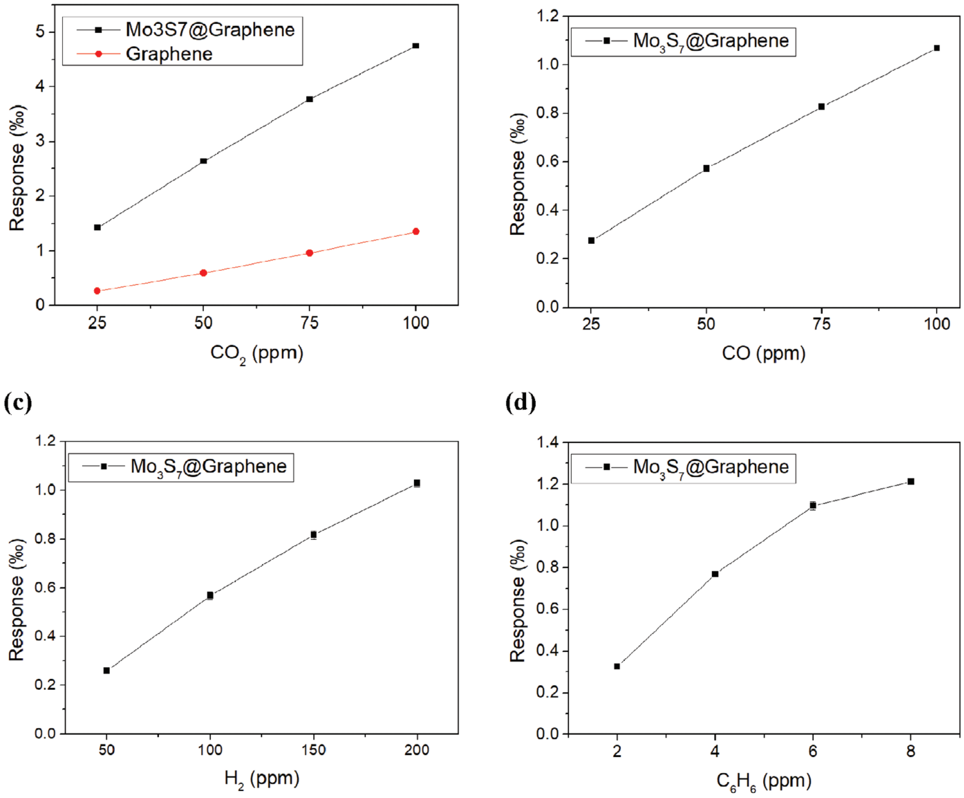

Figure 5. Calibration curves for CO_2 (a), CO (b), H_2 (c) and benzene (d) detection. Bare graphene can only effectively measure CO_2, while the graphene decorated with Mo_3S_7 clusters has been proven adequate for measuring all four gases.

between bare graphene (electrical responses in Figure S4, Supporting Information) and graphene decorated with the clusters. Notably, sensing responses demonstrate a four to five-fold enhancement for the decorated graphene compared to its bare counterparts. Additionally, considering sensor sensitivity as the slope of the calibration curve, the Mo_3S_7@Graphene sensor exhibits three times greater sensitivity than bare graphene (4.46×10^{-2} vs 1.45×10^{-2} ‰ ppm^{-1}). This indicates that the presence of Mo_3S_7 significantly enhances the sensing performance of the graphene-based gas sensor.

In addition to CO_2, other gases were measured using a similar methodology. Figure 4b,c depict the responses of Mo_3S_7@Graphene to four concentrations of CO (ranging from 25 to 100 ppm) and H_2 (ranging from 50 to 200 ppm), respectively. It can be observed that the decorated sensitive layer exhibits precise and repeatable responses to both gases. Conversely, bare graphene could not effectively measure these analytes (see Figure S4b,c, Supporting Information). In other words, as illustrated in **Figure** 5b,c, the calibration curves of bare graphene are absent due to unreliable responses derived from noisy measurements. This underscores the importance and impact of Mo_3S_7 clusters in enhancing the sensing performance.

Considering the sensitivity based on the slopes of the calibration curves, the CO sensitivity (1.05×10^{-2} ‰ ppm^{-1}) is twice that of H_2 (0.51×10^{-2} ‰ ppm^{-1}). Nevertheless, Mo_3S_7@Graphene still offers significantly higher sensitivity to CO_2 compared to CO (four times lower) and H_2 (approximately eight times lower). This reveals the particular sensitivity of Mo_3S_7 to CO_2, while detecting other gas compounds may pose a significant challenge in potential real-world scenarios owing to the cross-interference signals.

Finally, benzene was measured within a concentration range of 2 to 8 ppm. Figure 4d shows the dynamic responses, revealing a slight resistance baseline drift, suggesting that five minutes of dry air may not be sufficient to desorb all molecules. In consequence, this partial desorption may account for the slightly different baseline level observed in benzene compared to the other gases. Moreover, as depicted in Figure 5d, benzene is the only gaseous species lacking a linear calibration curve in the concentration range studied. This indicates that at the highest measured concentration (8 ppm), the Mo_3S_7@Graphene begins to show a saturated response, shifting from linear to second-order polynomial regression for calibration fitting. This complicates effective comparison with the previously tested gases, which displayed linear regression. In the case of benzene, bare graphene also proved incapable of measurement under the experimental conditions applied. Table S1–S4 (Supporting Information) summarize the values obtained for the different calibration curves.

It is worth highlighting that, apart from benzene, the Mo_3S_7@Graphene demonstrates high reversibility in its interaction with gas compounds, as evidenced by its rapid recovery to the initial resistance baseline and the absence of significant baseline drift. Moreover, the repeatability of the sensitivity layer is remarkable, with errors generally less than 1% across the various concentrations measured. Considering the remarkable sensing

Table 1. Summary of the limit of detection (LOD) and quantification (LOQ) obtained for different gas analytes employing the Mo_3S_7@Graphene sensor.

Analite	LOD [ppm]	LOQ [ppm]
CO_2	4.5	15.1
CO	6.1	20.3
H_2	9.9	32.9

performance of the Mo_3S_7@Graphene sensor, the limit of detection (LOD) and quantification (LOQ) were calculated as follows:

$$LOD = \frac{3S_a}{b} \tag{1}$$

$$LOQ = \frac{10S_a}{b} \tag{2}$$

where S_a is the standard deviation of the y-intercepts, while b corresponds to the slope of the calibration curve. **Table 1** summarizes the LOD and LOQ values obtained, demonstrating that the Mo_3S_7@Graphene sensor can reliably detect and quantify various target gases at low ppm levels. It is worth noting that these limits were calculated only for the gases that exhibited linear regressions. Consequently, benzene was excluded from the calculations due to the lack of linearity, likely caused by the observed baseline drift.

2.3. Sensing Mechanism

Regarding the registered resistance changes, the Mo_3S_7@Graphene layer behaves as a typical p-type semiconductor, wherein resistance increases upon interaction with electron donor gases. This phenomenon occurs because positive charges (holes) are the predominant carriers, and the incorporation of electrons from gaseous analytes leads to the recombination of electron–hole pairs, thus reducing the density of holes and consequently decreasing the conductivity of the sensitive film. While acknowledging the limited interaction between CO_2 and bare graphene, it is crucial to note that sensing responses are primarily attributed to the presence of Mo_3S_7 clusters. The electron-accepting properties of the trimetallic cluster and the direct anchoring on the graphene surface favor the electron transfer toward the resistive response.[19]

Theoretical calculations were performed under the density functional theory (DFT) framework for a better understanding of the interactions between the Mo_3S_7 clusters and the target molecules. Considering the best sensing performance of the Mo_3S_7@Graphene material toward CO_2, CO and H_2 molecules, these were chosen as the target gases in calculations. The $[Mo_3S_7Cl_6]^{2-}$ complex was taken as the most suitable and simplest model of the supported cluster on the graphene layer, since graphene acts as a spectator in the reactivity toward the gases and it is not expected that the cluster anchoring would affect drastically in the cluster electronic properties. The attack of each gas analyte to different cluster sites of the trimetallic cluster, namely, the $Mo_3/\mu_3\text{-}S/\mu\text{-}S_{eq}$, $Mo_3/\mu\text{-}S_{ax}$, and Mo_3/Cl_2 facets, was modeled in a 1:1 ratio to afford the respective $[\{Mo_3\text{-}\mu_3\text{-}S\}\cdots gas]$, $[\{Mo_3\text{-}\mu\text{-}S\}\cdots gas]$ and $[\{Mo_3\text{-}Cl_2\}\cdots gas]$ adducts (**Figure 6**). Since Mo atoms are coordinately saturated, no direct metal interaction with gases was envisaged. The interactions between the cluster compound and the gas molecule of each adduct were analyzed structurally and energetically. The energetic interactions were assessed by computing the BEs associated with the formation of each cluster-gas adduct.

An inspection of the structure of each cluster adduct involving CO_2 and CO show that these gases are oriented in a highly symmetric disposition to the cluster anion and interact through supramolecular interactions with the sulfur and chlorine atoms (Figure S5a,b, Supporting Information). For $[\{Mo_3\text{-}\mu_3\text{-}S\}\cdots CO_x]$ and $[\{Mo_3\text{-}\mu\text{-}S\}\cdots CO_x]$ (x = 1, 2) adducts, each carbonylated molecule is arranged in one of the three planes bisecting the Mo_3 unit. In the case of $[\{Mo_3\text{-}\mu_3\text{-}S\}\cdots CO_x]$, the plane contains the $\mu_2\text{-}S_2/\mu_3\text{-}S/Mo/Cl_2$ atoms, whereas for $[\{Mo_3\text{-}\mu\text{-}S\}\cdots CO_x]$, it comprises the $\mu_3\text{-}S/Mo/Cl_2$ atoms. For the $[\{Mo_3\text{-}Cl_2\}\cdots CO_x]$ adduct, the CO_x bisects the Mo-Cl_2 plane and is oriented approximately parallel to the trimetallic plane. An analysis of the supramolecular interactions involved in the cluster-CO_x adducts (Figure 6a,b) shows that, among the six structures, the closest gas-cluster distances found involve $O\cdots\mu\text{-}S_{eq}$ interactions in $[\{Mo_3\text{-}\mu_3\text{-}S\}\cdots CO_x]$ (x = 1, 3.544 Å, x = 2, 3.142 Å), and C···Cl interactions in $[\{Mo_3\text{-}Cl_2\}\cdots CO_x]$ (x = 1, CO, 3.517 Å; x = 2, 3.308 Å). The shortest interatomic distances found in $[\{Mo_3\text{-}\mu_3\text{-}S\}\cdots CO_2]$ and $[\{Mo_3\text{-}Cl_2\}\cdots CO_2]$ correspond to the highest BEs (−4.3 and −4.5 kcal mol^{-1}, respectively) among the calculated adducts (Table S5, Supporting Information), and are comparable to the BEs associated with CO_2 adsorbed on MoS_2 surfaces.[47,48] The longer interatomic distances found for the adducts involving the CO molecule and $[Mo_3S_7Cl_6]^{2-}$ are transduced in a slight decrease of the BEs (−3.3 kcal mol^{-1}), in agreement with the lower sensitivity registered in comparison to that obtained for CO_2. The BEs of the cluster adducts decrease drastically to less than 1 kcal mol^{-1} by changing the gas from carbonylated analytes to H_2 (Table S5, Supporting Information), in agreement with the decrease of resistive results observed experimentally. This behavior is explained by the weak H···Cl interactions observed in $[\{Mo_3\text{-}\mu_3\text{-}S\}\cdots H_2]$, $[\{Mo_3\text{-}\mu\text{-}S\}\cdots H_2]$ and $[\{Mo_3\text{-}Cl_2\}\cdots H_2]$ adducts (2.890, 2.839 and 3.164 (av) Å, respectively (Figure 6c; Figure S5c, Supporting Information), which imply a slight elongation of the Mo—Cl bonds (less than 0.05 Å). Among these adducts, the highest BE corresponds to $[\{Mo_3\text{-}Cl_2\}\cdots H_2]$, and it is attributed to the H···Cl interactions involved in the four-atom cycle formed between H_2 and the Mo-Cl_2 unit.

In all cases, BEs are negative, indicating that the formation of cluster-gas molecule adducts is exothermic (Table S5, Supporting Information). Thus, CO_2, CO and H_2 molecules are likely to be adsorbed onto the surface of the cluster-based material, to a higher or lesser extent.

3. Conclusion

A novel nanomaterial based on trinuclear molybdenum sulfido clusters supported on graphene was implemented in a single gas chemoresistive sensing device. The hybrid nanomaterial developed can work under room temperature conditions and can be

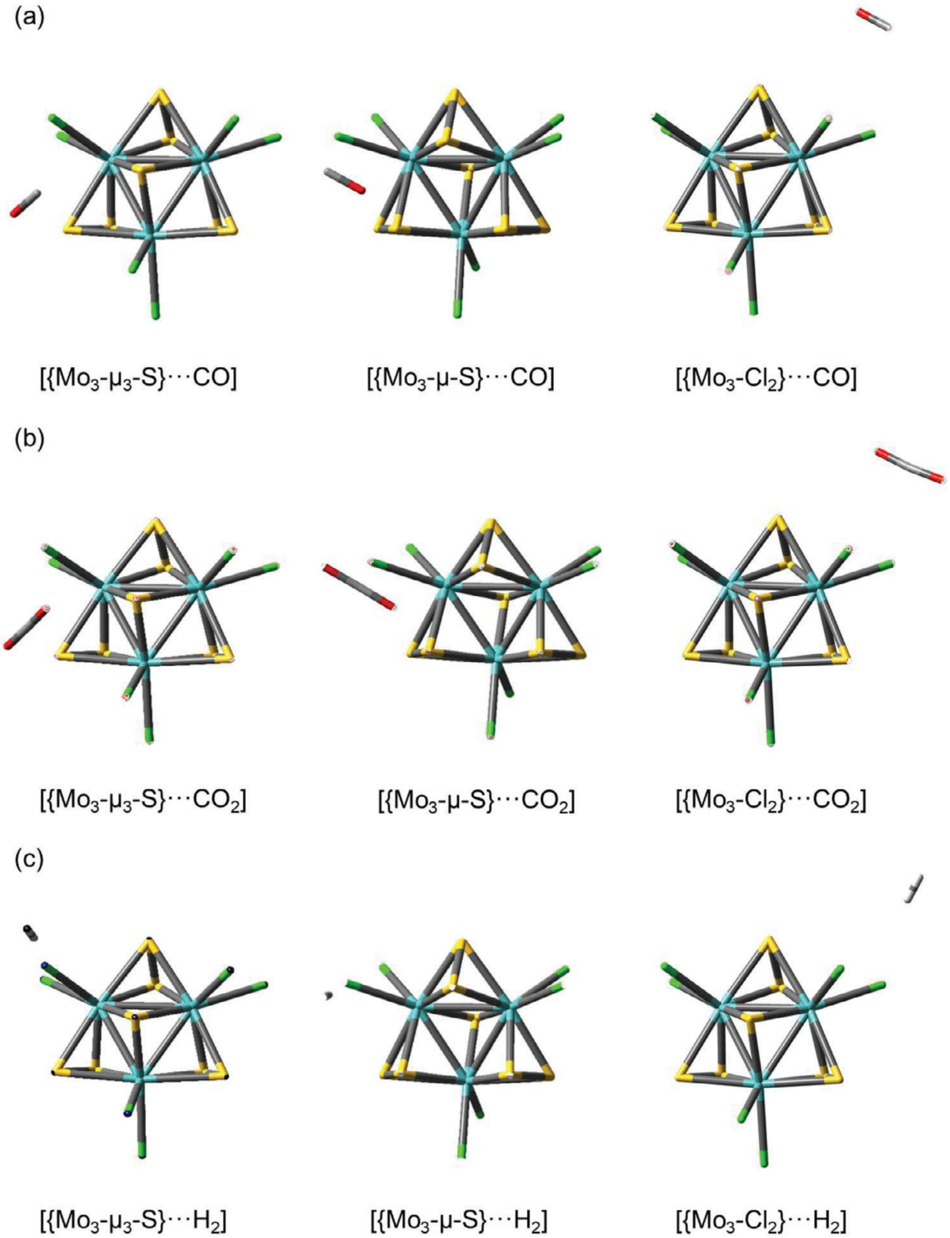

Figure 6. Schematic representation of the [{Mo_3-μ_3-S}···gas], [{Mo_3-μ-S}···gas] and [{Mo_3-Cl_2}···gas] (gas = CO (a), CO_2 (b) and H_2 (c)) adducts. Color code: Mo (blue), S (yellow), Cl (green), O (red), C (gray), and H (white).

easily integrated into miniaturized devices. The $[Mo_3(\mu_3\text{-}S)(\mu_2\text{-}S_2)_3]^{4+}$ cluster core, with chloridos as terminal ligands, is supported coordinatively onto the graphene layer, keeping the cluster robustness and electronic properties. The response to CO_2 is significantly improved by ≈5 times when graphene is decorated with the Mo_3S_7 clusters. Additionally, while bare graphene is unable to effectively detect gases like CO, H_2, and benzene, its functionalization with the Mo_3 sulfido clusters enhances its sensing performance, allowing for the detection of these gases. This is attributed to the grafting of the Mo-sulfur cluster cores onto the graphene layers. DFT calculations confirmed that the gas sensing mechanisms are based on supramolecular interactions between the analyte and the sulfur and chlorine cluster atoms of the octahedral cluster entities. This work reports for the first time trinuclear molybdenum sulfido clusters decorating graphene for sensing applications, thus contributing to the development of a new type of nanohybrids for detecting a wide variety of air pollutants.

4. Experimental Section

Synthesis of $(Bu_4N)_2[Mo_3(\mu_3\text{-}S)(\mu_2\text{-}S_2)_3Cl_6]\cdot 2H_2O$ *(*Mo_3S_7*)*: The synthesis of the molecular Mo_3S_7 cluster material was achieved by adapting a described procedure from the already prepared cluster precursor $(NH_4)_2[Mo_3S_{13}]\cdot nH_2O$ (n = 0–2).[33] In a typical procedure for preparation of Mo_3S_7, the $(NH_4)_2[Mo_3S_{13}]\cdot nH_2O$ cluster precursor (0.800 g, 1.05 mmol) was dispersed in HCl 37% (120 mL) and was heated under reflux for 4 h. The resulting mixture was filtered to remove the elemental sulfur generated during the reaction and afterward, Bu_4NCl was added in excess until precipitation of an orange solid. The reaction mixture was introduced in a cold bath and, after filtration, the solid was washed with water, methanol, and diethyl ether to give an orange crystalline material identified as Mo_3S_7 (1.064 g, yield 84%).

Mo_3S_7@Graphene Development and Sensing Device Fabrication: Two solutions were prepared in parallel to support the molybdenum clusters on graphene. First, a 10 mL graphene suspension (0.5 mg mL^{-1}) in dichloromethane was performed employing graphene nanoplatelets (750 $m^2\ g^{-1}$ surface area, Strem Chemicals Inc., USA). Then, the resulting suspension was placed in an ultrasonic tip to achieve proper graphene exfoliation. A pulsed sonication (1s on/2s off) at 280 W for 90 min was applied. A 1 mL solution of Mo_3S_7 (0.25 mg mL^{-1}) in dichloromethane was prepared. Afterward, the Mo_3S_7 solution was added to the graphene suspension and mixed for 10 min under stirring at room temperature, resulting in graphene loaded with a 5% wt. of Mo_3S_7 cluster. Subsequently, the mixture was homogenized by sonication for 1 h in an ultrasonic bath, resulting in a suitable distribution of molybdenum clusters supported on graphene (Mo_3S_7@Graphene). The resulting nanomaterial was deposited via spray coating. Specifically, the composite was deposited onto platinum screen-printed electrodes on alumina substrates. A moderate temperature (60 °C) was applied during the spray coating deposition, and nitrogen was used as a carrier gas to avoid cluster degradation.

Characterization Techniques: The Raman spectra were obtained from solid samples previously deposited onto quartz substrates, using a "Reflex" Renishaw spectrometer, equipped with an Olympus microscope. The exciting wavelengths were 514 and 785 nm of an Ar^+ ion laser, while the laser power was ≈10–25 mW; 20 acquisitions were taken for each spectrum. Powder X-ray diffraction patterns were obtained using a Philips X′Pert diffractometer and copper radiation ($CuK\alpha$ = 1.541178 Å). X-ray photoelectron (XPS) spectra were collected over a sample deposited onto a copper coated steel foil and using a SPECS spectrometer with a 150MCD-9 detector and using a non-monochromatic $AlK\alpha$ (1486.6 eV) X-Ray source. Spectra were recorded using an analyzer pass energy of 30 eV, an X-ray power of 100 W and under an operating pressure of 10^{-9} mbar. During data processing of the XPS spectra, BE values were referenced to the C1s peak (284.5 eV). Spectra treatment and peak fitting was performed using the CASA software. Samples for high-resolution electron microscopy (HR-TEM) were ultrasonically dispersed in Milli-Q water and transferred into carbon-coated copper grids. HR-TEM images were recorded using a JEOL JEM2100F microscope operating at 200 kV. HR-FESEM images were recorded with a Zeiss GeminiSEM 500 apparatus (Zeiss-Oxford Instruments) with an accelerating voltage of 5.0 kV. The interlaminar spacing in HR-TEM images was determined using Gatan Microscopy Suite software.

Resistive Gas Sensing Measurements: The gas sensors were placed in a sealed Teflon chamber (volume of 35 cm^3), which is connected to a gas delivery system employing calibrated gas cylinders alongside pristine dry air, ensuring a purity level of 99.999% (Air Premier standard). The resistance levels were monitored under constant measurement employing a multimeter (HP 34972A, Agilent). To minimize power usage and replicate realistic experimental settings to the maximum extent, the overall airflow was regulated to a low rate (100 mL min^{-1}) through a combination of mass-flow controllers (Bronkhorst High-Tech B.V.) and electrovalves. Before exposure to specific gaseous concentrations, the sensors were allowed a 5-min stabilization period in dry air. Subsequently, successive target gas dilutions were applied, defining the sensor response as $\Delta R/R_0$, presented as a percentage. ΔR represents the resistance changes observed over a 1-min gas exposure period, while R_0 refers to the sensor baseline resistance in air.

Computational Details: The calculations were conducted with the Gaussian 09 program suite. Density functional theory was applied with the PBE0 functional.[49,50] Relativistic electron core potentials (RECP) from the Stuttgart group and its associated basis sets (SDDALL)[51] were used to represent the molybdenum[52] and the iodine atoms[52] and augmented, in the case of Mo, by an f polarization function (Mo: $\alpha = 1.043$)[53] and in the case of S and Cl, with a d polarization function (S: $\alpha = 0.503$; Cl: $\alpha = 0.640$).[54] The 6–31G(d,p) basis set was used to represent the remaining atoms (O, C and H) of the molecular systems. The geometry optimizations were performed in the gas phase without any symmetry constraint followed by analytical frequency calculations to confirm that a minimum has been reached. Stability between adducts was analyzed by calculating relative electronic energies (E_{rel}) or difference of electronic energies between the selected adduct and the most stable adduct. Zero-point energies were included in BE calculations, and the BEs were calculated using $BE = E_{(cluster\text{-}molecule)} - [E_{cluster} + E_{molecule}]$.

Supporting Information

Supporting Information is available from the Wiley Online Library or from the author.

Acknowledgements

J.C.-C. gratefully acknowledges the Marie Skłodowska-Curie Individual Fellowship (Horizon Europe Program), grant agreement No. 101066282 "GREBOS." E.L. is supported by the Catalan Institution for Research and Advanced Studies via the 2023 Edition of the ICREA Academia Award. M.F. acknowledges the financial support by the Spanish Ministry of Science and Innovation (TED2021-130963B-C21 and CEX2021-001230-S grants) funded by MCIN/AEI/10.13039/501100011033 and FEDER A way of making Europe, and funding for open access charge: CRUE-Universitat Politècnica de València. The authors gratefully acknowledge Ana Moreno Muñoz and Maria Adelina Muñoz Algaba for their assistance in the characterization of the samples. The Electron Microscopy Service of the UPV is also acknowledged for their help in spectroscopic identification. M.F. thanks Prof. Rosa Llusar for her comments on this work.

Conflict of Interest

The authors declare no conflict of interest.

Data Availability Statement

The data that support the findings of this study are available from the corresponding author upon reasonable request.

Keywords

gas detection, graphene, molybdenum sulfido cluster, resistive sensor

Received: July 6, 2024
Revised: August 29, 2024
Published online: September 25, 2024

---

[1] G. O. Ofremu, B. Y. Raimi, S. O. Yusuf, B. A. Dziwornu, S. G. Nnabuife, A. M. Eze, C. A. Nnajiofor, *Green Energy Resour.* **2024**, 100074.
[2] K. Kamboj, S. Sisodiya, A. K. Mathur, A. Zare, P. Verma, *Water, Air, Soil Pollut.* **2022**, *233*, 82.
[3] S. M. Majhi, A. Mirzaei, H. W. Kim, S. S. Kim, T. W. Kim, *Nano Energy* **2021**, *79*, 105369.
[4] R. J. Rath, W. B. Zhang, O. Kavehei, F. Dehghani, S. Naficy, S. Farajikhah, F. Oveissi, *ACS Sens.* **2024**, *9*, 1735.

[5] M. Galvani, S. Freddi, L. Sangaletti, *Sensors* **2024**, *24*, 584.
[6] D. Balram, K.-Y. Lian, N. Sebastian, V. Kumar, V. K. Yadav, A. Patel, K. Singh, *Sensors Int.* **2024**, *5*, 100269.
[7] X. Tian, S. Wang, H. Li, M. Li, T. Chen, X. Xiao, Y. Wang, *Sensors & Diagnostics* **2023**, *2*, 361.
[8] N. Goel, K. Kunal, A. Kushwaha, M. Kumar, *Eng. Reports* **2023**, *5*, e12604.
[9] R. Kumar, W. Zheng, X. Liu, J. Zhang, M. Kumar, *Adv. Mater. Technol.* **2020**, *5*, 1901062.
[10] R. K. Jha, N. Bhat, *Adv. Mater. Interfaces* **2020**, *7*, 1901992.
[11] H. Rhyu, S. Lee, M. Kang, D. Yoon, S. Myung, W. Song, S. S. Lee, J. Lim, *RSC Adv.* **2023**, *13*, 13128.
[12] J. Wang, Z. Ji, G. Yang, X. Chuai, F. Liu, Z. Zhou, C. Lu, W. Wei, X. Shi, J. Niu, L. Wang, H. Wang, J. Chen, N. Lu, C. Jiang, L. Li, M. Liu, *Adv. Funct. Mater.* **2018**, *28*, 1806244.
[13] F. Ricciardella, K. Lee, T. Stelz, O. Hartwig, M. Prechtl, M. McCrystall, N. McEvoy, G. S. Duesberg, *ACS Omega* **2020**, *5*, 5959.
[14] P. Pham, G. Li, E. Bekyarova, M. E. Itkis, A. Mulchandani, *ACS Nano* **2019**, *13*, 3196.
[15] S. Guo, D. Yang, S. Zhang, Q. Dong, B. Li, N. Tran, Z. Li, Y. Xiong, M. E. Zaghloul, *Adv. Funct. Mater.* **2019**, *29*, 1900138.
[16] J. Casanova-Chafer, R. Garcia-Aboal, P. Atienzar, M. Feliz, E. Llobet, *ACS Appl. Mater. Interfaces 14*, 57122.
[17] V. E. Fedorov, Y. V. Mironov, N. G. Naumov, M. N. Sokolov, V. P. Fedin, *Russ. Chem. Rev.* **2007**, *76*, 529.
[18] R. Llusar, C. Vicent, *Coord. Chem. Rev.* **2010**, *254*, 1534.
[19] A. L. Gushchin, Y. A. Laricheva, M. N. Sokolov, R. Llusar, *Russ. Chem. Rev.* **2018**, *87*, 670.
[20] D. Recatalá, R. Llusar, F. Galindo, K. A. Brylev, A. L. Gushchin, *Eur. J. Inorg. Chem.* **2015**, *2015*, 1877.
[21] V. P. Fedin, J. Czyzniewska, R. Prins, T. Weber, *Appl. Catal. A Gen.* **2001**, *213*, 123.
[22] A. Rajagopal, F. Venter, T. Jacob, L. Petermann, S. Rau, S. Tschierlei, C. Streb, *Sustain. Energy Fuels* **2019**, *3*, 92.
[23] M. Dave, A. Rajagopal, M. Damm-Ruttensperger, B. Schwarz, F. Nägele, L. Daccache, D. Fantauzzi, T. Jacob, C. Streb, *Sustain. Energy Fuels* **2018**, *2*, 1020.
[24] Y. Lei, M. Yang, J. Hou, F. Wang, E. Cui, C. Kong, S. Min, *Chem. Commun.* **2018**, *54*, 603.
[25] J. Kibsgaard, T. F. Jaramillo, F. Besenbacher, *Nat. Chem.* **2014**, *6*, 248.
[26] Y. Shang, X. Xu, B. Gao, Z. Ren, *ACS Sustainable Chem. Eng.* **2017**, *5*, 8908.
[27] Y. Wang, P. Dong, K. Zhu, A. Zhang, J. Pan, Z. Chen, Z. Li, R. Guan, X. Xi, J. Zhang, *Chem. Eng. J.* **2022**, *446*, 136883.
[28] I. Romanenko, A. Rajagopal, C. Neumann, A. Turchanin, C. Streb, F. H. Schacher, *J. Mater. Chem. A* **2020**, *8*, 6238.
[29] P. T. Hung, P. D. Hoat, V. X. Hien, H.-Y. Lee, S. Lee, J.-H. Lee, J.-J. Kim, Y.-W. Heo, *ACS Appl. Mater. Interfaces* **2020**, *12*, 34274.
[30] D. Fadil, J. Sharma, M. I. Rizu, E. Llobet, *ACS Omega* **2024**, *9*, 25297.
[31] M. Zhang, F. Grasset, Y. Masubuchi, T. Shimada, T. K. N. Nguyen, N. Dumait, A. Renaud, S. Cordier, D. Berthebaud, J.-F. Halet, T. Uchikoshi, *Nanomaterials* **2023**, *13*, 478.
[32] J. Casanova-Chafer, R. Garcia-Aboal, E. Llobet, P. Atienzar, *ACS Sens.* **2024**, *9*, 830.
[33] V. P. Fedin, M. N. Sokolov, Y. V. Mironov, B. A. Kolesov, S. V. Tkachev, V. Y. Fedorov, *Inorganica Chim. Acta* **1990**, *167*, 39.
[34] M. A. Kuroda, J. Tersoff, R. A. Nistor, G. J. Martyna, *Phys. Rev. Appl.* **2014**, *1*, 14005.
[35] A. Müller, V. Wittneben, E. Krickemeyer, H. Bögge, M. Lemke, *Zeitschrift für Anorg. und Allg. Chemie* **1991**, *605*, 175.
[36] T. Weber, J. C. Muijsers, J. W. Niemantsverdriet, *J. Phys. Chem.* **1995**, *99*, 9194.
[37] J. C. Muijsers, T. Weber, R. M. Vanhardeveld, H. W. Zandbergen, J. W. Niemantsverdriet, *J. Catal.* **1995**, *157*, 698.
[38] P. D. Tran, T. V. Tran, M. Orio, S. Torelli, Q. D. Truong, K. Nayuki, Y. Sasaki, S. Y. Chiam, R. Yi, I. Honma, J. Barber, V. Artero, *Nat. Mater.* **2016**, *15*, 640.
[39] S. Batool, S. P. Nandan, S. N. Myakala, A. Rajagopal, J. S. Schubert, P. Ayala, S. Naghdi, H. Saito, J. Bernardi, C. Streb, A. Cherevan, D. Eder, *ACS Catal.* **2022**, *12*, 6641.
[40] M. J. Mayor-López, J. Weber, K. Hegetschweiler, M. D. Meienberger, F. Joho, S. Leoni, R. Nesper, G. J. Reiss, W. Frank, B. A. Kolesov, V. P. Fedin, V. E. Fedorov, *Inorg. Chem.* **1998**, *37*, 2633.
[41] S. A. Adonin, A. V. Virovets, M. N. Sokolov, V. P. Fedin, *Russ. J. Coord. Chem.* **2010**, *36*, 871.
[42] A. Gushchin, R. Llusar, D. Recatalá, P. Abramov, *Russ. J. Coord. Chem.* **2012**, *38*, 173.
[43] W. Li, Y. Li, K. Xu, *Nano Lett.* **2021**, *21*, 1150.
[44] D. Bouša, J. Luxa, V. Mazánek, O. Jankovský, D. Sedmidubský, K. Klímová, M. Pumera, Z. Sofer, *RSC Adv.* **2016**, *6*, 66884.
[45] V. P. Fedin, Y. V. Mironov, A. V. Virovets, N. V. Podberezskaya, V. Y. Fedorov, *Polyhedron* **1992**, *11*, 2083.
[46] M. N. Sokolov, O. A. Gerasko, S. F. Solodovnikov, V. P. Fedin, *J. Struct. Chem.* **2004**, *45*, 490.
[47] J. Cao, Q. Chen, X. Wang, Q. Zhang, H.-D. Yu, X. Huang, W. Huang, *Res.* **2021**, *2021*, 1.
[48] C. González, B. Biel, Y. J. Dappe, *Phys. Chem. Chem. Phys.* **2017**, *19*, 9485.
[49] J. P. Perdew, K. Burke, M. Ernzerhof, *Phys. Rev. Lett.* **1996**, *77*, 3865.
[50] C. Adamo, V. Barone, *J. Chem. Phys.* **1999**, *110*, 6158.
[51] D. Andrae, U. Häußermann, M. Dolg, H. Stoll, H. Preuß, *Theor. Chim. Acta* **1990**, *77*, 123.
[52] M. Dolg, U. Wedig, H. Stoll, H. Preuss, *J. Chem. Phys.* **1987**, *86*, 866.
[53] A. W. Ehlers, M. Böhme, S. Dapprich, A. Gobbi, A. Höllwarth, V. Jonas, K. F. Köhler, R. Stegmann, A. Veldkamp, G. Frenking, *Chem. Phys. Lett.* **1993**, *208*, 111.
[54] A. Höllwarth, M. Böhme, S. Dapprich, A. W. Ehlers, A. Gobbi, V. Jonas, K. F. Köhler, R. Stegmann, A. Veldkamp, G. Frenking, *Chem. Phys. Lett.* **1993**, *208*, 237.